

Sub-kpc star formation law in the local luminous infrared galaxy IC 4687 as seen by ALMA

M. Pereira-Santaella^{1,2}, L. Colina^{1,2}, S. García-Burillo³, P. Planesas³, A. Usero³, A. Alonso-Herrero⁴, S. Arribas^{1,2}, S. Cazzoli^{1,2}, B. Emonts^{1,2}, J. Piqueras López^{1,2}, and M. Villar-Martín^{1,2}

Centro de Astrobiología (CSIC/INTA), Ctra de Torrejón a Ajalvir, km 4, 28850, Torrejón de Ardoz, Madrid, Spain
e-mail: mpereira@cab.inta-csic.es, ASTRO-UAM, UAM, Unidad Asociada CSIC, Observatorio Astronómico Nacional (OAN-IGN)-Observatorio de Madrid, Alfonso XII, 3, 28014, Madrid, Spain, Instituto de Física de Cantabria, CSIC-Universidad de Cantabria, E-39005 Santander, Spain

Preprint online version: March 29, 2021

ABSTRACT

We analyze the spatially resolved (250 pc scales) and integrated star formation (SF) law in the local luminous infrared galaxy (LIRG) IC 4687. This is one of the first studies of the SF law on a starburst LIRG at these small spatial scales. We combined new interferometric ALMA CO(2–1) data with existing *HST*/NICMOS Pa α narrowband imaging and VLT/SINFONI near-IR integral field spectroscopy to obtain accurate extinction-corrected SF rate (SFR) and cold molecular gas surface densities (Σ_{gas} and Σ_{SFR}). We find that IC 4687 forms stars very efficiently with an average depletion time (t_{dep}) of 160 Myr for the individual 250 pc regions. This is approximately one order of magnitude shorter than the t_{dep} of local normal spirals and also shorter than that of main-sequence high- z objects, even when we use a Galactic α_{CO} conversion factor. This result suggests a bimodal SF law in the $\Sigma_{\text{SFR}} \propto \Sigma_{\text{gas}}^N$ representation. A universal SF law is recovered if we normalize the Σ_{gas} by the global dynamical time. However, at the spatial scales studied here, we find that the SF efficiency (or t_{dep}) does not depend on the local dynamical time for this object. Therefore, an alternative normalization (e.g., free-fall time) should be found if a universal SF law exists at these scales.

Key words. Galaxies: starburst — Galaxies: star formation

1. Introduction

There is a strong correlation between the star formation rate (SFR) and the cold molecular gas content in galaxies. This relation is usually referred to as the star formation (SF) law (or as the Kennicutt-Schmidt relation; Schmidt 1959; Kennicutt 1998) and it is expressed as

$$\Sigma_{\text{SFR}} = A \Sigma_{\text{gas}}^N, \quad (1)$$

where Σ_{SFR} and Σ_{gas} are the SFR and cold molecular gas surface densities, respectively. For galaxy integrated observations, the typical power-law index, N , is 1.4–1.5 (Kennicutt 1998; Yao et al. 2003). The physical processes leading to this value of N are not well established yet, although theoretical models suggest that variations of the free-fall time (t_{ff}) and the orbital dynamical time might define the observed relation (see McKee & Ostriker 2007 and Kennicutt & Evans 2012 for a review).

In general, it is assumed that the normalization of the SF law, A , is constant, that is, independent of the galaxy type. However, some works have found bimodal SF laws when main sequence (MS) and starbursts (those with higher specific SFR than MS galaxies for a given redshift) are considered (e.g., Daddi et al. 2010; Genzel et al. 2010; García-Burillo et al. 2012). In these cases, normal galaxies have depletion times ($t_{\text{dep}} = M_{\text{H}_2}/\text{SFR}$) between 4 and 10 times longer than starburst galaxies. The possible existence of this bimodality in the SF law affects the determination of N . Actually, these works find an almost linear relation,

$N \sim 1$, for each galaxy population (MS and starbursts) when they are treated independently.

Recently, many studies of the resolved sub-kpc SF laws in nearby galaxies have appeared (e.g., Kennicutt et al. 2007; Bigiel et al. 2008; Leroy et al. 2008; Verley et al. 2010; Rahman et al. 2012; Viaene et al. 2014; Casasola et al. 2015). Most of these works find a wide range of N values (0.8–2.3) and a considerable scatter in the relations (0.1–0.4 dex). This could be explained if the SF law breaks down on sub-kpc scales (e.g., the location of the cold molecular gas peaks, CO, and the SFR regions, H α , are not always coincident; Kennicutt et al. 2007; Schrubba et al. 2010) and/or because some systematics affect these sub-kpc studies (e.g., the treatment of the diffuse background emission; Liu et al. 2011).

These previous sub-kpc studies are focused on very nearby ($d < 20$ Mpc) spiral galaxies and active galactic nuclei (AGN). That is, the only objects where sub-kpc resolutions could be achieved before the arrival of the Atacama Large Millimeter/submillimeter Array (ALMA). Therefore, the most extreme local starbursts (i.e., luminous and ultra-luminous IR galaxies) are absent in previous sub-kpc studies, although they are important to understand extreme high- z SF (e.g., Daddi et al. 2010).

In this paper, we present one of the first sub-kpc analyses of the SF law in a local extreme starburst. In particular, we study the local ($d=74$ Mpc; 345 pc arcsec^{−1}) luminous IR galaxy (LIRG) IC 4687. This galaxy has an IR luminosity of $10^{11.3} L_{\odot}$, which corresponds to an integrated SFR of

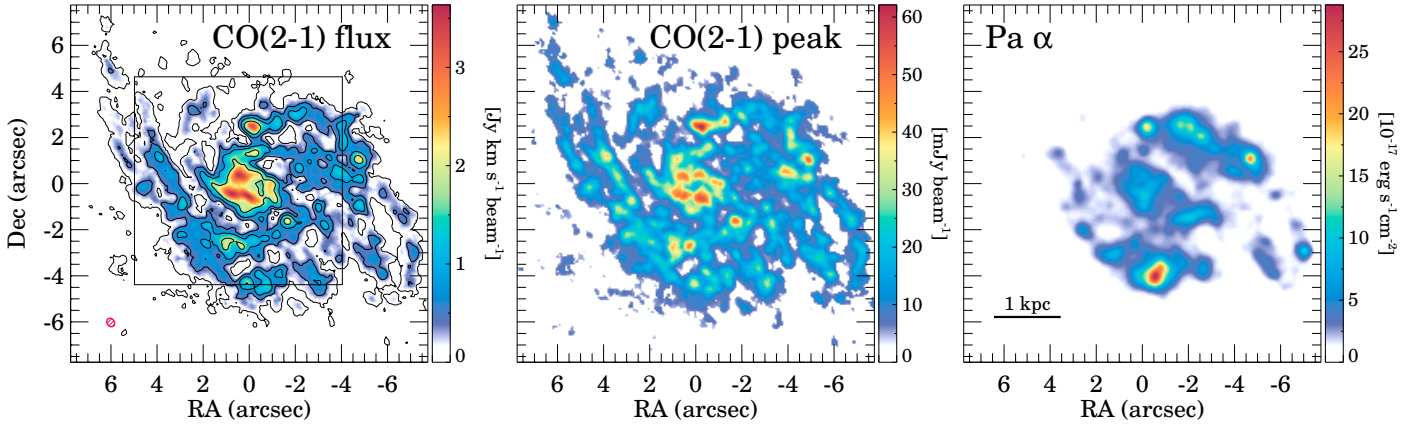


Fig. 1. ALMA $^{12}\text{CO}(2-1)$ integrated flux and peak intensity for $\sim 5 \text{ km s}^{-1}$ channels (left and middle panels) and *HST*/*NICMOS* $\text{Pa}\alpha$ map smoothed to the ALMA resolution (right panel) of IC 4687. The contour levels of the left panel indicate the 10, 100, 200, and 400 σ levels. The 1σ sensitivity of the data is 1 mJy beam^{-1} for $\sim 5 \text{ km s}^{-1}$ channels. The red hatched ellipse in the left panel indicates the ALMA beam size ($0''.31 \times 0''.39$, PA 35°). The black square indicates the field of view covered by the VLT/SINFONI data, i.e., the region to which we restricted our analysis in this paper.

$\sim 30 M_\odot \text{ yr}^{-1}$ (Pereira-Santaella et al. 2011). Although, the energy output of IC 4687 is dominated by SF, a weak AGN with a contribution $< 5\%$ to the total IR luminosity, is possibly present (Alonso-Herrero et al. 2012). IC 4687 forms part of an interacting group together with IC 4686 and IC 4689, which are ~ 10 and $\sim 20 \text{ kpc}$ away from IC 4687, respectively. Both IC 4687 and IC 4689 are spiral-like galaxies with ordered velocity fields that are dominated by rotation and kinematic centers coincident with their optical continuum peaks. Only the less massive galaxy of the system (IC 4686) shows a velocity field dominated by a tidal tail (see Bellocchi et al. 2013 for details). Therefore, the starburst of IC 4687 might be induced by this weak interaction.

We obtained new ALMA $^{12}\text{CO}(2-1)$ observations with $\sim 100 \text{ pc}$ spatial resolution to study the SF law in IC 4687. We combined these observations with *HST*/*NICMOS* maps of $\text{Pa}\alpha$ (50 pc resolution; Alonso-Herrero et al. 2006) and VLT/SINFONI near-IR integral field spectroscopy (200 pc resolution; Piqueras López et al. 2012, 2013, 2015, submitted). This multi-wavelength dataset allowed us to get a novel insight into the sub-kpc SF law in extreme local starbursts. In addition, optical integral field spectroscopy data of the entire IC 4686/4687/4689 system have recently been obtained (Rodríguez-Zaurín et al. 2011; Bellocchi et al. 2013; Arribas et al. 2014; Cazzoli et al. 2015, submitted), but they were not considered in the present analysis because of their different spatial resolution.

This paper is organized as follows: We describe the observations and data reduction in Section 2. The analysis of the cold molecular gas and SFR maps of IC 4687 are presented in Section 3. In Sections 4 and 5, we discuss our results in the context of nearby and high- z galaxies, respectively. Finally, in Section 6, we summarize the main findings of the paper.

2. Observations and data reduction

2.1. $^{12}\text{CO}(2-1)$ ALMA data

We obtained band 6 observations of IC 4687 with ALMA on August 28 2014 and April 5 2015 using extended and

compact antenna array configurations with 35 and 39 antennas, respectively (project 2013.1.00271.S; PI: L. Colina). The on-source integration times were 18 and 9 min, respectively. Both observations were single pointing centered at the nucleus of IC 4687. The extended configuration had baselines between 33.7 m and 1.1 km, while the baselines ranged between 15.1 m and 328 m for the compact configuration. For these baselines, the maximum recoverable scales are $4.9''$ and $10.9''$, respectively.

Two spectral windows of 1.875 GHz bandwidth ($0.48 \text{ MHz} \sim 0.6 \text{ km/s}$ channels) were centered at the sky frequencies of $^{12}\text{CO}(2-1)$ (226.4 GHz) and $\text{CS}(5-4)$ (240.7 GHz). In addition, two continuum spectral windows were set at 228.6 and 243.4 GHz . In this paper, we only present the analysis of the $\text{CO}(2-1)$ data.

The two datasets were calibrated using the standard ALMA reduction software CASA (v4.2.2; McMullin et al. 2007). We used J1617-5848 for the amplitude calibration, assuming a flux density of 0.651 Jy at 226.4 GHz , and Titan, using the Butler-JPL-Horizons 2012 model, for the extended and compact configurations, respectively. The uv visibilities of each observation were converted to a common frequency reference frame (kinematic local standard of rest; LRSK) and then combined. The amplitudes of the baselines in common for both array configurations were in good agreement. Then, the continuum ($0.15\text{--}0.05 \text{ mJy beam}^{-1}$) was fitted with the line free channels and subtracted in the uv plane. In the final data cubes, we used 4 MHz channels ($\sim 5 \text{ km s}^{-1}$) and 256×256 pixels of $0''.07$. For the cleaning, we used the Briggs weighting with a robustness parameter of 0.5 (Briggs 1995), which provided a beam with a full width half maximum (FWHM) of $0''.31 \times 0''.39$ ($\sim 100 \text{ pc} \times 130 \text{ pc}$) with a position angle (PA) of 35° . A mask derived from the observed $\text{CO}(2-1)$ emission in each channel was used during the clean process. For the final 4 MHz channels, the achieved 1σ sensitivity is $\sim 1 \text{ mJy beam}^{-1}$. We applied the primary beam correction to the data cubes.

The integrated $\text{CO}(2-1)$ flux in the considered ALMA field of view ($18'' \times 18''$) is 460 Jy km s^{-1} with a flux calibration uncertainty about 15%. For comparison, the single-dish $\text{CO}(2-1)$ flux measured with the 15 m SEST telescope

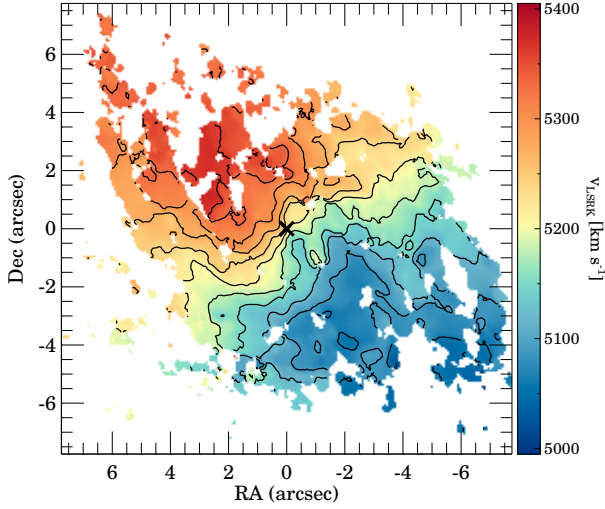


Fig. 2. CO(2–1) isovelocity contours in steps of 30 km s^{-1} from $v(\text{LSRK}) = 5000$ to 5400 km s^{-1} . The black cross indicates the kinematic center.

($24''$ beam size) is 480 Jy km s^{-1} (Albrecht et al. 2007). Therefore, combining both the compact and the extended ALMA array configurations we are able to recover most of the CO(2–1) flux of this source.

2.2. Ancillary HST/NICMOS and VLT/SINFONI data

We used the continuum subtracted narrowband Pa α HST/NICMOS image of IC 4687 (Alonso-Herrero et al. 2006) to determine the resolved SFR. The original Pa α map ($0''.15$ resolution) was convolved with a Gaussian kernel to match the angular resolution of the ALMA map. To correct the Pa α emission for extinction (see next section), we used the 2D extinction maps of this galaxy derived with near-IR VLT/SINFONI integral field spectroscopy (Piqueras López et al. 2013, 2015, submitted). Both the ALMA CO(2–1) and the NICMOS Pa α maps cover similar fields of view. However, we limited our analysis to the smaller field of view of the SINFONI extinction map ($8'' \times 8''$; see Figure 1) so the dataset would be homogeneously corrected for extinction. Nevertheless, this region contains $\sim 85\%$ of the total CO(2–1) flux.

We calculated the position of the dynamical center of the CO(2–1) emission by locating the maximum of the directional derivative of the velocity field (Figure 2; see also Arribas et al. 1997). Then, we aligned the peak of the stellar mass distribution traced by the NICMOS and SINFONI near-IR continuum with the CO(2–1) dynamical center.

3. Analysis and results

3.1. Molecular and ionized gas morphology

In Figure 1, we show the Pa α and CO(2–1) integrated flux and peak intensity maps of IC 4687. Four spiral-like arcs are visible in the molecular gas emission. The two more external arms are also evident in the Pa α map (see also Figure 3). The Pa α emission of the southern arc is dominated by a bright $\sim 1 \text{ kpc}$ in diameter region, while in the northern arm it is spread over $\sim 3 \text{ kpc}$ along the arc.

There is a 1 kpc diameter ring of molecular gas around the nucleus. This ring is spatially coincident with the

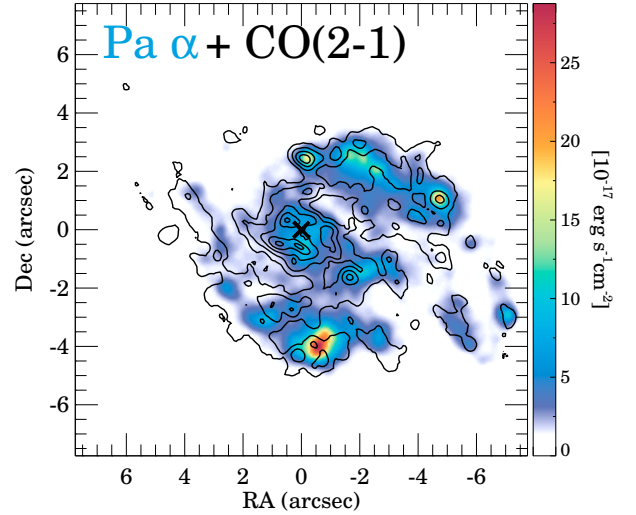


Fig. 3. CO(2–1) integrated emission contours overlaid on the Pa α emission map of IC 4687. Both maps are shown at the same spatial resolution. The black cross indicates the kinematic center. The contour levels of the CO(2–1) integrated flux correspond to 0.43 , 1.1 , 1.9 , 2.8 , and $3.4 \text{ Jy km s}^{-1} \text{ beam}^{-1}$.

brightest, hot H $_2$ emission (Piqueras López et al. 2012). This ring is relatively weak in the observed Pa α emission. This is mainly because of the higher extinction of the nuclear ring with respect to the rest of SF regions (see Section 3.2).

Figure 3 shows the comparison of the Pa α and CO(2–1) emissions. The general agreement is good. As stated above, both the Pa α and CO(2–1) emissions trace similar spiral arcs and a circumnuclear ring, however, on scales of 100 pc the CO(2–1) and Pa α emission peaks do not always coincide. There are regions where the Pa α emission is strong and there is no clear CO(2–1) peak associated with the emission, while other regions detected in the CO(2–1) maps do not show Pa α emission.

3.2. Characterization of the regions

We used the integrated CO(2–1) emission map to define individual emitting regions. Emission peaks above a 10σ level were considered. This conservative σ level was chosen to exclude residual side lobes produced by the bright central region. We applied the same procedure to the Pa α map and then we combined both sets of regions.

In Figure 4, we plot the location of these 81 regions. We assumed that regions with centroids separated by less than $0''.35$ (ALMA beam) in the CO and Pa α maps correspond to the same physical region. Using this criterion, 23 regions are detected in both the CO(2–1) and Pa α maps. There are 43 and 15 regions detected only in the CO or Pa α maps, respectively. Both CO(2–1) and Pa α emissions are detected at more than 6σ for all these regions, although an emitting clump is seen only in one of the maps. The diameter of the regions was fixed to $0''.7$ (~ 2 times the ALMA beam), which corresponds to $\sim 250 \text{ pc}$ at the distance of IC 4687. This physical scale is ideal for comparison with previous works (see Section 4).

To measure the CO(2–1) emission of each region, we extracted their spectra and integrated all the channels above

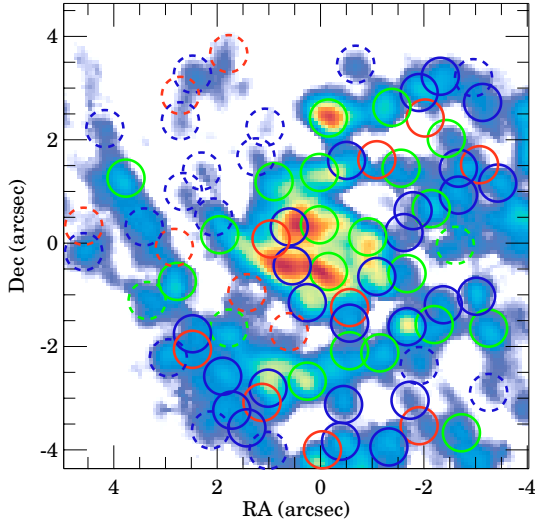


Fig. 4. Location of the apertures defined for IC 4687 overlaid on the CO(2–1) map. Blue and red circles indicate apertures only detected at $>10\sigma$ in the CO(2–1) or the Pa α maps, respectively. Green circles indicate regions with both CO(2–1) and Pa α emission peaks detected at $>10\sigma$ level. Dashed circles indicate regions whose Br γ or Br δ emissions are detected below a 6σ level.

a 3σ level within the velocity range of the CO(2–1) emission in this object ($5000\text{--}5400\text{ km s}^{-1}$). We estimated the cold molecular gas mass from the CO(2–1) emission using the Galactic CO-to- H_2 conversion factor, $\alpha_{\text{CO}}^{1-0} = 4.35$ (Bolatto et al. 2013; see Section 3.3.3), and the CO(2–1) to CO(1–0) ratio (R_{21}) of 0.7 derived from the single-dish CO data of this galaxy (Albrecht et al. 2007). This R_{21} value is similar to that found by Leroy et al. (2013) in nearby spiral galaxies. Using this conversion factor, the molecular gas surface density ranges from $10^{2.3}$ to $10^{3.4} M_{\odot} \text{ pc}^{-2}$ within the 250 pc of diameter apertures. This corresponds to molecular masses of the individual regions in the range $M_{\text{H}_2} = 10^7 - 10^8 M_{\odot}$, so they likely include several giant molecular clouds.

We estimated the SFR of the regions using the extinction corrected Pa α emission. First, we performed aperture photometry on the Pa α image for each region. To correct the Pa α emission for extinction, we used the Br γ /Br δ ratio map of Piqueras López et al. (2013) and assumed an intrinsic Br γ /Br δ ratio of 1.52 (Hummer & Storey 1987) and the Fitzpatrick (1999, F99) extinction law. This A_K determination is very sensitive to the uncertainty in the Br δ and Br γ fluxes. Therefore, we only considered regions where both the Br δ and Br γ transitions are detected at $>6\sigma$. Using this criterion, our final sample includes 54 out of the 81 original regions. Almost 90% of the regions detected in both the CO and Pa α maps fulfill this criterion, while $\sim 40\%$ of the regions detected only in CO or Pa α are excluded. Most of the excluded regions are those at the low-end of the CO and Pa α luminosity distributions. This suggests that we are limited by the sensitivity of the Br δ and Br γ maps, which would be lower than that of the ALMA and HST/NICMOS data.

The measured extinction range is $A_K = 0.2\text{--}3.5$ mag ($A_V = 2\text{--}30$ mag) with a median A_K of 1.3 mag ($A_V = 11$ mag). Correcting the observed Pa α emission by this median extinction yields an extinction-corrected

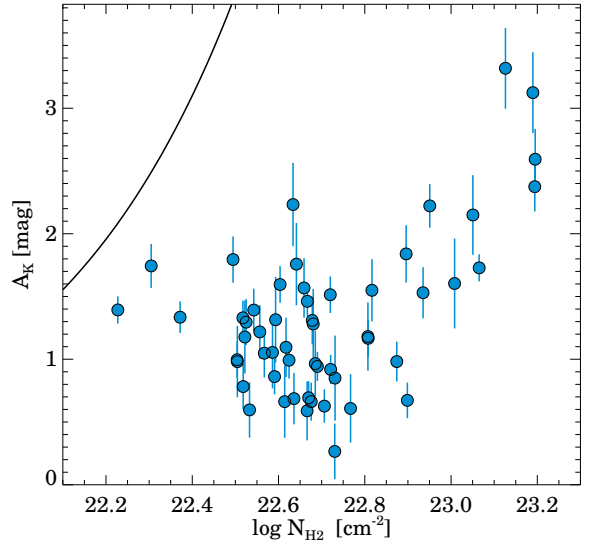


Fig. 6. Relation between the H_2 column density (N_{H_2}) and the extinction (A_K) in IC 4687 for the 250 pc regions. The solid black line corresponds to $N_{\text{H}_2}/A_K = 8.1 \times 10^{21} \text{ cm}^{-2} \text{ mag}^{-1}$ (Bohlin et al. 1978).

flux that is ~ 4 times the observed flux. We show the spatial distribution of A_K in the left panel of Figure 5. The most obscured regions ($A_K > 1.7$ mag) are located at the ring of molecular gas around the nucleus, while the regions in the arms have lower A_K values. The extinction-corrected Pa α luminosities of the regions were converted into SFR following the Kennicutt & Evans (2012) calibration for H α (assuming H α /Pa α = 8.58; Hummer & Storey 1987). For this SFR calibration, Kennicutt & Evans (2012) adopted the Kroupa (2001) initial mass function. The SFR surface density in this galaxy is $1\text{--}100 M_{\odot} \text{ yr}^{-1} \text{ kpc}^{-2}$ for the 250 pc regions. All of these Σ_{H_2} and Σ_{SFR} values are multiplied by $\cos 47^\circ$ to correct for the inclination of this galaxy ($i = 47^\circ$; Bellocchi et al. 2013).

3.3. Systematic uncertainties

Both the SFR and the cold molecular gas surface density estimates are affected by several systematic effects. These effects have been widely studied in the past (e.g., Rahman et al. 2011; Liu et al. 2011; Schruba et al. 2011; Bolatto et al. 2013; Genzel et al. 2013; Casasola et al. 2015). Therefore, in this section, we briefly discuss the possible systematic effects due to the region selection, SFR tracer, extinction correction, and CO-to- H_2 conversion factor we used.

3.3.1. Region selection

In the local spiral M 33, for physical scales of 300 pc, Schruba et al. (2010) found that the depletion time (t_{dep}) is shorter by a factor of ~ 3 for apertures centered on H α peaks than for apertures centered on CO peaks. For IC 4687, the average $\log t_{\text{dep}}/\text{yr}$ is 8.3 ± 0.3 and 8.2 ± 0.4 for the CO and Pa α selected regions, respectively. That is, we do not see any significant difference between the CO and Pa α selected regions with the 250 pc apertures in this galaxy in terms of t_{dep} . Therefore, in the following, we do not distinguish between CO and Pa α selected regions.

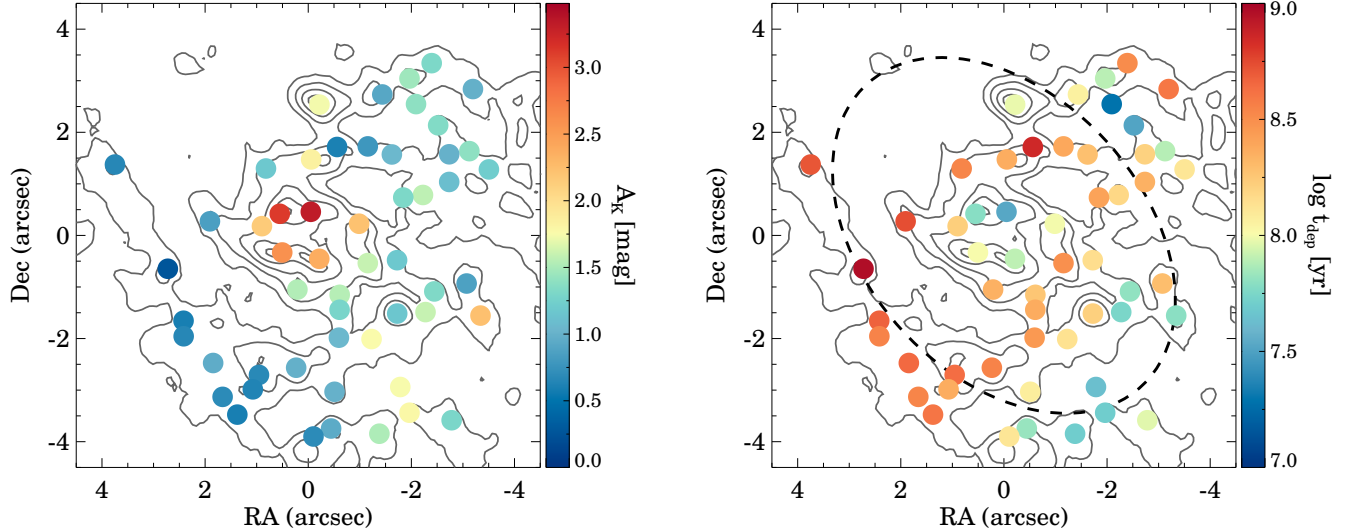


Fig. 5. Spatial distribution of the A_K (left) and t_{dep} (right) of the regions. The contours represent the CO(2–1) emission as in Figure 3. The dashed ellipse in the right panel represents the orbit with a dynamical time of 50 Myr (see Section 4.4).

3.3.2. Extinction correction and SFR tracer

We used the Galactic F99 extinction law to correct for dust obscuration effects on IC 4687. This choice is appropriate because we use hydrogen recombination lines ($\text{Pa}\alpha$, $\text{Br}\delta$, and $\text{Br}\gamma$) to derive A_K values ($A_V = 8.6 \times A_K$). We also tried the Calzetti et al. (2000) extinction law. Both laws have similar $A_K/A_{\text{Pa}\alpha}$ ratios (~ 1.3), but we find that A_K values derived using the Calzetti et al. (2000) law are ~ 2.2 times lower than following the Galactic law. This is owing to the steeper slope of this law in the range $1.9\text{--}2.2\ \mu\text{m}$ where the $\text{Br}\gamma$ and $\text{Br}\delta$ transitions lie. This difference only affects very obscured regions ($A_K^{\text{F99}} > 2\text{ mag}$) where the SFR derived assuming the Calzetti et al. law would be ~ 3 times lower.

Near-IR transitions yield higher A_K (or A_V) values than optical transitions (e.g., Balmer decrement). This is because the relative contribution of highly obscured regions to the total line emission is higher for the near-IR lines. Therefore, the equivalent A_V estimated from near-IR lines is higher as well. Consequently, SF laws depend on how the extinction correction is applied. For instance, using optical tracers, the derived SFR varies up to a factor of 10 for extremely obscured galaxies and for the slope of the SF laws (e.g., Genzel et al. 2013). In the near-IR, the extinction effects are greatly reduced, so for our case, we estimate that the uncertainties due to the application of the extinction correction are only a factor of ~ 2 for the A_K range of this object.

In addition, extinction corrections can be performed region by region or using an average A_K value. For IC 4687, we find that the results are similar on average when using the region-by-region extinction and the integrated extinction (see Section 5). However, like Genzel et al. (2013), we find that the relation between the SFR and cold molecular gas is flatter if we use an average extinction value. This is because of the relation between the A_K and the H_2 column density (Figure 6). Regions with more cold molecular gas are more extinguished, so they are undercorrected when we apply the average extinction. Therefore, the relation be-

tween the SFR and the cold molecular gas is flatter when the average A_K is assumed.

Finally, to check the extinction correction applied, in Figure 6 we plot the relation between the H_2 column density, which is derived from the Σ_{H_2} values, and A_K . In Galactic regions there is a correlation between these two quantities (Bohlin et al. 1978; Pineda et al. 2010). In IC 4687, this trend is relatively weak (Spearman’s rank correlation coefficient $r_s = 0.30$, probability of no correlation $p = 0.04$), although, as expected, regions with higher H_2 column densities tend to have higher A_K . In particular, this occurs for regions with $A_K > 1.6\text{ mag}$ and $\log N_{\text{H}_2}(\text{cm}^{-2}) > 22.7$. For lower A_K and N_{H_2} values, this relation disappears in IC 4687 at these spatial scales. For comparison, we also plot in Figure 6 the Galactic relation as a solid line. The measured A_K values in IC 4687 are systematically lower than the Galactic prediction by factor of ~ 6 . This suggests that the dust properties and/or geometry of the star-forming regions of this object differ from those found in Galactic regions. In Section 3.3.3, we explain that the Galactic α_{CO} factor is favored for IC 4687. However, we emphasize that using the α_{CO} of ULIRGs, which is 5–7 times lower than the Galactic α_{CO} factor (Bolatto et al. 2013), would reconcile the observed H_2 column densities and A_K with the Galactic relation.

3.3.3. CO-to- H_2 conversion factor

The derived cold molecular gas masses depend on the α_{CO} conversion factor used. In Section 3.2, we assumed that the Galactic α_{CO} factor is a good choice for IC 4687. However, we could expect a lower conversion factor, similar to that of ULIRGs, in this galaxy because of its high specific SFR ($\text{sSFR} = \text{SFR}/\text{stellar mass}$), $\sim 0.4\text{ Gyr}^{-1}$ (Pereira-Santaella et al. 2011). Genzel et al. (2015) proposed that galaxies with high sSFR, that is, galaxies that lie above the MS of SF galaxies, have reduced α_{CO} factors. IC 4687 has a $\text{sSFR} \sim 6$ times higher than a local MS galaxy with the same stellar mass (Whitaker et al. 2012). Therefore, using the α_{CO} factor of ULIRGs could be justified.

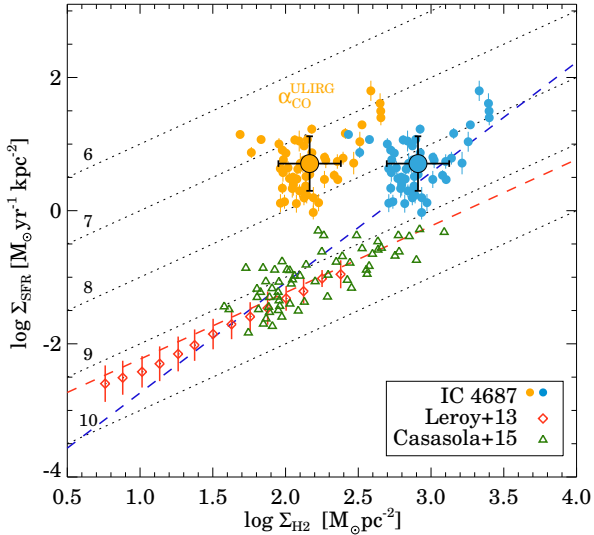


Fig. 7. SFR surface density as function of the molecular gas surface density. The circles correspond to the 250 pc regions defined for IC 4687 (Section 3.2). For the orange circles we applied the CO-to-H₂ conversion factor of local ULIRGs, while for the blue circles we applied the Milky Way conversion factor. The large circles indicate the average values for the IC 4687 regions. The green triangles and red diamonds indicate spatially resolved measurements in nearby galaxies by Casasola et al. (2015) and Leroy et al. (2013), respectively. The molecular gas tracer for all of them is the CO(2–1) transition. The dotted lines mark constant $\log t_{\text{dep}}$ times. The dashed blue line is the best fit to all the data ($N=1.6$), and the dashed red line represents the best fit excluding the IC 4687 data ($N=1.0$).

However, it is not clear if the integrated CO-to-H₂ conversion factor of ULIRGs, where CO emission is not likely confined to individual molecular clouds (Bolatto et al. 2013), applies to our 250 pc regions in IC 4687. In addition, IC 4687 is not a strongly interacting galaxy or a merger like most local ULIRGs (Figure 1); it has a velocity field dominated by rotation (Figure 2), although it is perturbed by noncircular motions. In addition, the morphology of the CO emission of IC 4687 resembles that of a normal spiral galaxy (see Leroy et al. 2008) with the SF spread over a region of several kpc. Therefore, it is possible that the cold molecular gas properties (turbulence, temperature, and density) of IC 4687 differ from those of local ULIRGs where a lower α_{CO} factor is required. In fact, in a single-dish survey of local U/LIRGs, Papadopoulos et al. (2012) found that near-Galactic α_{CO} values for U/LIRGs are possible when the contribution from high density gas ($n > 10^4 \text{ cm}^{-3}$) is taken into account. Also, in the case of IC 4687, if we used the α_{CO} of ULIRGs, the t_{dep} of the regions would be extremely short, that is, almost 100 times shorter than those of local spiral galaxies (see Section 4.1).

4. Comparison with local galaxies

In Figure 7, we compare the spatially resolved (200–500 pc) SFR and molecular gas surface densities of nearby galaxies presented by Leroy et al. (2008) and Casasola et al. (2015) with those of IC 4687. Leroy et al. (2008) studied a sample of 23 nearby ($d < 15 \text{ Mpc}$) normal spiral galaxies, while

Casasola et al. (2015) studied four nearby ($d < 20 \text{ Mpc}$) low-luminosity AGN.

Figure 7 shows that IC 4687 regions have high molecular gas surface densities, $\log \Sigma_{\text{H}_2} (\text{M}_\odot \text{ pc}^{-2}) = 2.9 \pm 0.2$, close to the high end of the Σ_{H_2} distribution observed in nearby active galaxies. Moreover, the IC 4687 regions form stars more rapidly than normal galaxies do. These regions have $\log \Sigma_{\text{SFR}} (\text{M}_\odot \text{ yr}^{-1} \text{ kpc}^{-2}) = 0.7 \pm 0.4$, which is a factor of ~ 10 higher than the most extreme values measured in nearby galaxies. This is consistent with the general behavior of local LIRGs, as their H II regions are typically a factor of 10 more luminous than those in normal star-forming galaxies (Alonso-Herrero et al. 2002, 2006). Consequently, the t_{dep} of the IC 4687 regions is $160^{+750}_{-140} \text{ Myr}$ (average $\log t_{\text{dep}}/\text{yr} = 8.2 \pm 0.4$). This is approximately one order of magnitude shorter than in nearby galaxies, which is 1–2 Gyr (Bigiel et al. 2008, 2011; Leroy et al. 2013; Casasola et al. 2015) for similar physical scales.

4.1. Systematic uncertainties

In this section, we use data from the local studies of Leroy et al. (2008) and Casasola et al. (2015). Leroy et al. (2008) used the H α +24 μm luminosities to derive the SFR, so our results are directly comparable. Casasola et al. (2015) instead used the extinction-corrected H α luminosity. They used the integrated P α /H α ratio to derive this correction, so we expect their SFR to be systematically underestimated when compared to ours (Section 3.3.2). Since their galaxies are less extinguished ($A_K \sim 0.2 \text{ mag}$) than the LIRG IC 4687, we estimate that this difference is less than a factor of 2.

These local studies assume a Galactic CO-to-H₂ conversion factor, which is the adopted factor for IC 4687. Consequently, if this factor is valid for IC 4687, all the cold molecular gas surface density comparisons should be consistent. However, in Figure 7, we also plot the SF law assuming an α_{CO} factor typical of ULIRGs (Downes & Solomon 1998) for IC 4687. Using this factor, the molecular gas masses and depletion times are reduced by a factor of ~ 5 . Therefore, the regions in IC 4687 would have Σ_{H_2} similar to those of normal galaxies, but $\Sigma_{\text{SFR}} \sim 100$ times higher. Actually, if we apply the α_{CO} factor of ULIRGs to IC 4687, this galaxy would be an extreme starburst compared to local and high- z galaxies (Section 5). In principle, we do not expect such extreme behavior in a weakly interacting spiral galaxy such as IC 4687. Therefore, we consider the Galactic α_{CO} factor preferred for IC 4687.

4.2. Higher star formation efficiency?

On average, the SF regions of the LIRG IC 4687 have higher cold molecular gas surface densities than those in other nearby galaxies measured on similar spatial scales when assuming the same α_{CO} (Figure 7). There is some overlap, however, with the regions measured by Casasola et al. (2015) in the range $M_{\text{H}_2} = 10^{2.5} - 10^{3.1} \text{ M}_\odot \text{ pc}^{-2}$.

If the SFR were linearly correlated with the amount of molecular gas (see e.g., Bigiel et al. 2008), we would expect higher SFR densities in IC 4687, but also similar depletion times. However, the depletion times in IC 4687 are 10 times shorter than in nearby galaxies. Therefore, for IC 4687, the

SFR surface density does not follow the relation observed in nearby galaxies, even in overlapping mass range.

Alternatively, a nonlinear SF law fits the data with a power-law index of $N = 1.6$ (Figure 7), which is similar to the indexes derived for galaxy integrated data (see Section 1). However, if we exclude the IC 4687 data from the fit, a linear relation is recovered. That is, the nonlinearity of the relation is only due to the IC 4687 regions. Sub-kpc resolved observations of more extreme starbursts will be needed to determine if they follow a nonlinear SF law or if the SF efficiency (SFE) is actually bimodal since it is more efficient in starburst galaxies (see Section 5.4).

4.3. Dispersion of t_{dep} in IC 4687

We find that the t_{dep} scatter within IC 4687 regions is relatively high, at 0.4 dex. A similar, although slightly lower, dispersion of the t_{dep} values is found in nearby galaxies observed at similar spatial resolution (Leroy et al. 2013; Casasola et al. 2015). In addition, in IC 4687 (Figure 7) the correlation between the molecular gas and the SFR surface densities is weak ($r_s = 0.24$, $p = 0.08$). This suggests that, on scales of 250 pc, the relation between the SFR and the cold molecular gas breaks in this galaxy, or at least, it is hidden by the scatter.

Some works (e.g., Onodera et al. 2010; Schrubba et al. 2010; Kruijssen & Longmore 2014) argue that the time evolution of the SF regions plays a key role in explaining the t_{dep} scatter when high spatial resolution data is used. Actually, at high spatial resolution (75 pc) the distributions of the CO and ionized gas emissions are different (e.g., Schrubba et al. 2010). This is also partially true on scales of 130 pc for IC 4687 (Figure 3). Therefore, the evolutionary state of the molecular clouds in IC 4687 could give rise to the scatter in the SFR vs. cold molecular gas relation. With the current observations, however, it is not possible to establish the evolutionary state of the regions in IC 4687, so we cannot test this hypothesis.

Additional scatter is produced by the selected SFR tracers (e.g., Schrubba et al. 2011). We use the extinction-corrected Pa α emission as a tracer of the SFR. The Pa α traces the ionizing radiation produced by young stars and it is detectable for clusters younger than ~ 10 Myr (Kennicutt & Evans 2012). Therefore, our SFR estimates are only sensitive to recent SF (< 10 Myr), which might be more variable than the SFR averaged over longer time periods (~ 100 Myr) traced by the UV or IR continuum (e.g., Schrubba et al. 2011; Casasola et al. 2015). This short-term SFR variability can also produce part of the scatter seen in Figure 7.

Finally, when the mass of the young SF regions is low ($< 10^5 M_\odot$), the incomplete sampling of the IMF can induce large variations in the SFR tracers (e.g., Verley et al. 2010). To test this effect, we estimated the mass of the young stars in each region from the Pa α luminosity. For an instantaneous burst of SF, the STARBURST99 code (Leitherer et al. 1999) provides the ionizing radiation produced by a cluster as a function of time. Therefore, assuming that the regions of IC 4687 are close to the peak of the ionizing radiation production (i.e., 0–3 Myr old), we determine that these young clusters have stellar masses between $10^{5.5}$ and $10^7 M_\odot$ (these are lower limits if the regions are older than 3 Myr; see also Alonso-Herrero et al. 2002). Cerviño et al. (2002) showed that for young clusters more massive than $10^5 M_\odot$ (stellar mass) the uncertainties due to the IMF

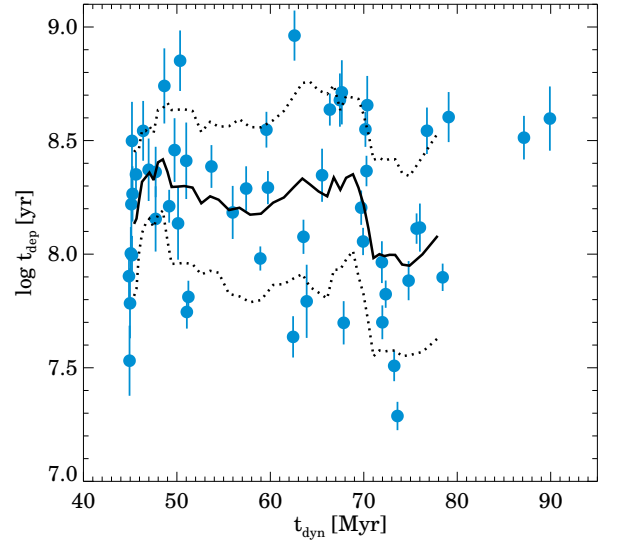


Fig. 8. Depletion time (t_{dep}) as a function of the local dynamical time (t_{dyn}). The solid black line indicates the running average t_{dep} value over ten regions. The dotted lines represent the 1σ dispersion of this average.

sampling are less than 25 %. Consequently, it is not likely that the IMF sampling has any effect on the correlation shown in Figure 7 at the SFR level of IC 4687 using 250 pc apertures.

4.4. Local dynamical time

An alternative formulation of the SF law uses the dynamical time (or orbital time $= 2\pi r/v_{\text{rot}}$) to normalize the molecular gas surface density (e.g., Kennicutt et al. 2007). This formulation uses an average dynamical time for integrated measurements; it is able to recover a universal SF law valid for objects with high SFE, such as ULIRGs or sub-mm galaxies, and for normal spirals (see also Section 5.4).

For our resolved observations, it is possible to estimate the dynamical time of each region from their deprojected radius (assuming $i = 47^\circ$ and a major axis PA of 39°) and the rotation curve derived by Bellocchi et al. (2013) using kinemetry (Krajinović et al. 2006). In Figure 8, we show that the depletion time (or SFE) does not depend on the dynamical time ($r_s = 0.02$, $p = 0.86$). In the right panel of Figure 5, we show the spatial distribution of depletion times where no clear trends are seen. This absence of correlation is also seen in resolved observations of normal spirals (Leroy et al. 2008). Therefore, the local dynamical time does not seem to influence the local SFE at spatial scales of ~ 250 pc.

5. Comparison with high- z galaxies

5.1. Integrated properties of IC 4687

The SF laws derived for high- z galaxies are mostly based on integrated measurements. Therefore, it is useful to calculate the integrated properties of IC 4687 using an approach comparable to high- z studies.

We limited our integrated study to the $3 \times 3 \text{ kpc}^2$ area covered by the field of view of SINFONI (see Section 2) to obtain an accurate measurement of the extinction. This area contains about 85% of the total CO(2–1) and 90%

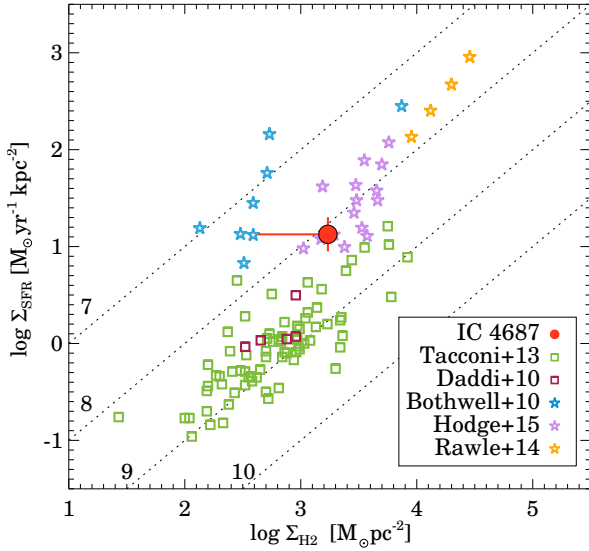


Fig. 9. Comparison of the SFR surface density as a function of the molecular gas surface density for high- z MS and sub-mm galaxies and IC 4687. The red circle indicates the integrated measurement for IC 4687, as described in Section 5, using the Galactic α_{CO} factor. The error bars indicate systematic uncertainties due to the extinction correction in Σ_{SFR} (vertical) and a change in the α_{CO} factor from Galactic (assumed) to that considered for ULIRGs (horizontal; see Section 3.3). The green and red squares correspond to $z \sim 1.2$ and 2.2 MS SF galaxies from Tacconi et al. (2013) and BzK $z \sim 1.5$ galaxies from Daddi et al. (2010). For both datasets we used the Galactic α_{CO} factor. The blue, purple, and orange stars correspond to sub-millimeter galaxies at $z \sim 2$, 4.0 , and 5.2 from Bothwell et al. (2010), Hodge et al. (2015), and Rawle et al. (2014), respectively, for which a ULIRG-like α_{CO} factor was applied. The dotted lines indicate constant $\log t_{\text{dep}}$ times.

of the observed $\text{Pa}\alpha$ emissions. Therefore, by limiting our analysis to this area, we only miss 10–15% of the total emission.

We derived an integrated extinction of $A_K = 1.2 \pm 0.1$ mag ($A_V = 10.1 \pm 0.8$ mag) based on the integrated $\text{Br}\gamma/\text{Br}\delta$ ratio. The total SFR, $43 \pm 4 M_\odot \text{ yr}^{-1}$, is calculated from the extinction-corrected $\text{Br}\gamma$ integrated flux¹ because the *HST*/NICMOS $\text{Pa}\alpha$ image is not sensitive to diffuse $\text{Pa}\alpha$ emission due to its small pixel size; this diffuse emission would be included in integrated measurements of high- z objects. This SFR is ~ 1.5 times higher than that derived from the IR luminosity, but this difference is within the assumed systematic uncertainties (see Section 3.3). From the integrated CO(2–1) emission, we derive a total cold molecular gas mass of $5.5 \times 10^9 M_\odot$.

In IC 4687, the extinction-corrected $\text{Pa}\alpha$ emission from the regions defined in Section 3.2 accounts for $\sim 70\%$ of the integrated SFR derived here. For the cold molecular gas, $\sim 65\%$ of the CO(2–1) emission comes from these regions. These two fractions are similar. Therefore, the integrated t_{dep} agrees with the average t_{dep} of the individual regions.

The effective CO(2–1) emitting area (that containing 50% of the total CO(2–1) emission) has a $R_{1/2}$ of 1.0 kpc,

¹ This $\text{Br}\gamma$ flux is multiplied by 12.1 (Storey & Hummer 1995) to obtain the $\text{Pa}\alpha$ equivalent flux.

which corresponds to an $\sim 30\%$ lower area than that of the individual regions combined. Therefore, because of the increased integrated CO(2–1) and $\text{Pa}\alpha$ fluxes from diffuse emission and the lower emitting area estimate, both the integrated SFR and cold molecular gas surface densities are ~ 2 times higher than the average values of the resolved regions in IC 4687, although the depletion times are similar.

5.2. High- z counterparts of IC 4687

In Figure 9, we compare the integrated SF law of IC 4687 with those obtained for MS $z \sim 1.2$ – 2.2 galaxies (Tacconi et al. 2013), $z \sim 1.5$ BzK galaxies (Daddi et al. 2010), and submillimeter galaxies (Bothwell et al. 2010; Rawle et al. 2014; Hodge et al. 2015).

We find that the integrated H_2 and SFR surface densities of IC 4687 lie at the high end of the distributions of values measured for high- z MS galaxies. The Σ_{SFR} and Σ_{H_2} values directly depends on the size of the emitting region, which is not easy to estimate for integrated galaxies (see Section 5.1 and Arribas et al. 2012). The depletion time, however, is independent of the emitting region size. Therefore, we focus on the t_{dep} differences in this section.

A galaxy with the sSFR of IC 4687 ($\text{sSFR} = \sim 0.4 \text{ Gyr}^{-1}$) would be a MS galaxy at $z \sim 0.9$ (see Section 3.3.3). As shown in Figure 9, high- z MS galaxies, in general, are less efficient than IC 4687 forming stars. On average, they have t_{dep} that are 6 times longer than IC 4687 (using the Galactic α_{CO} for IC 4687). Therefore, even if these $z = 1.2$ – 2.2 galaxies have sSFR, SFR, and stellar masses similar to IC 4687, they are more similar to local starbursts in terms of t_{dep} (Tacconi et al. 2013). This can be explained by the correlation between the t_{dep} and the sSFR normalized by the sSFR of a MS galaxy between $z = 0$ and 3 (Genzel et al. 2015). Since, the sSFR of IC 4687 is ~ 6 times higher than the local MS sSFR (Section 3.3.3), we expect a shorter depletion time in this local LIRG than in MS galaxies, at least for $z < 3$.

On the other hand, the t_{dep} of IC 4687 is similar to that of high- z sub-mm galaxies (Rawle et al. 2014; Hodge et al. 2015; Figure 9). The amount of cold molecular gas in IC 4687 and these sub-mm galaxies is also similar ($\sim 10^{10} M_\odot$), however, this depends on the CO-to- H_2 conversion used. For the sub-mm galaxies, the α_{CO} used is similar to that of local ULIRGs, that is, it is lower than the Galactic α_{CO} used for IC 4687. Consequently, if we would apply the ULIRG α_{CO} factor to IC 4687, its t_{dep} would be at the high end of the t_{dep} range measured in high- z sub-mm galaxies (Figure 9).

5.3. Systematic uncertainties

For high- z galaxies, the SFR is mainly obtained from the spectral energy distribution fitting. This kind of analysis includes the IR emission, therefore it is possible that our SFR derived from the $\text{Pa}\alpha$ luminosity are underestimated by a factor of two (see Piqueras López et al. 2015, submitted). The α_{CO} factor applied to high- z galaxies depends on the object class (Galactic factor for MS galaxies; ULIRG-like factor for sub-mm galaxies). Therefore, the comparison with the molecular gas surface density of IC 4687 is somewhat uncertain. For reference, in Figure 9 we represent the

range of Σ_{H_2} assuming the Galactic and ULIRG α_{CO} factors.

5.4. Bimodal SF law

Some studies have shown that the SF laws have a bimodal behavior with a factor 3–4 lower t_{dep} in local U/LIRGs than in normal SF galaxies (e.g., Daddi et al. 2010; Genzel et al. 2010; García-Burillo et al. 2012). We observe this bimodal behavior when we compare MS galaxies (Figures 7 and 9) with IC 4687.

To recover a universal SF law for integrated measurements of galaxies, several alternative formulations are proposed. We discuss two of them here. The first is to normalize the cold molecular gas surface density by the dynamical time ($\Sigma_{\text{H}_2}/t_{\text{dyn}}$; Silk 1997; Tan 2000). When this normalization is applied to integrated measurements, a global t_{dyn} is used (e.g., Kennicutt 1998; Daddi et al. 2010). In this case, the global dynamical times of U/LIRGs (~ 45 Myr) are 4–5 times shorter than those of spirals (~ 370 Myr), so the lower t_{dep} values of U/LIRGs are compensated and a universal relation between Σ_{SFR} and $\Sigma_{\text{H}_2}/t_{\text{dyn}}$ is obtained (e.g., Genzel et al. 2010; García-Burillo et al. 2012). The dynamical time of the outer regions of IC 4687 is ~ 80 Myr. Consequently, IC 4687 would lie in this universal relation as well (cf. equation 21 in García-Burillo et al. 2012).

In Section 4.4, we showed that the SFE does not depend on the local t_{dyn} in IC 4687. Thus, SF does not seem to be strongly affected by the local effects of the disk rotation. Therefore, the normalization by the global t_{dyn} might be a simplification of the physical mechanisms leading to this universal SF law relation.

Alternatively, the free-fall time is another proposed normalization for the cold molecular gas surface density ($\Sigma_{\text{H}_2}/t_{\text{ff}}$; Krumholz & McKee 2005) to recover a universal SF law. The t_{ff} is proportional to $1/\rho^{0.5}$, where ρ is the molecular gas volume density (Binney & Tremaine 1987). Therefore, systems with higher ρ have lower t_{ff} . If the molecular gas density is higher in U/LIRGs than in normal spirals (Gao & Solomon 2004), the t_{ff} normalization would recover a universal relation as well.

6. Conclusions

We have analyzed the resolved (250 pc scales) and integrated SF law in the local LIRG IC 4687. This is one of the first studies of the SF laws on a starburst dominated LIRG at these spatial scales. We combined new interferometric ALMA CO(2–1) observations with existing *HST*/NICMOS $\text{Pa}\alpha$ narrowband imaging and VLT/SINFONI near-IR integral field spectroscopy to obtain accurate cold molecular gas masses and extinction-corrected SFR estimates. The main conclusions of our analysis are the following:

1. We defined 54 regions with a diameter of 250 pc centered at the CO and $\text{Pa}\alpha$ emission peaks. The resolved Σ_{H_2} values of IC 4687 lie at the high end of the values observed in local galaxies at these spatial resolutions. Whereas the Σ_{SFR} are almost a factor of 10 higher than those of local galaxies for similar Σ_{H_2} . For the resolved regions of IC 4687, the correlation between Σ_{H_2} and Σ_{SFR} is weak ($r_s = 0.25$, $p = 0.08$). This suggests that the SF law breaks downs in this galaxy on scales of 250 pc.

2. Compared with resolved SF laws in local galaxies, IC 4687 forms stars more efficiently. The range of t_{dep} of the individual regions is 20–900 Myr with an average of 160 Myr. This is almost one order of magnitude shorter than that of local galaxies. For these estimates, we used a Galactic α_{CO} conversion factor; using an ULIRG-like factor would make the t_{dep} even shorter by an additional factor of 4–5.
3. The 1σ scatter in the t_{dep} values is 0.4 dex. We suggest that this can be due to the rapid time evolution of the SFR tracer we used ($\text{Pa}\alpha$). We rule out that the IMF sampling causes the observed scatter for this galaxy because of the high young stellar masses ($10^{5.5-7} M_{\odot}$) of the studied regions. We also show that the local dynamical time does not significantly affect the SF efficiency in IC 4687 (up to ~ 1.5 kpc away from the nucleus).
4. The galaxy integrated $\log \Sigma_{\text{H}_2} (M_{\odot} \text{pc}^{-2}) = 2.6 - 3.2$ and $\log \Sigma_{\text{SFR}} (M_{\odot} \text{yr}^{-1} \text{kpc}^{-2}) = 1.1 \pm 0.2$ of IC 4687 make this object have a $t_{\text{dep}} \sim 6$ times shorter than MS high- z galaxies. The Σ_{H_2} lies at the high end of the Σ_{H_2} distribution of high- z MS objects, whereas the Σ_{SFR} is ~ 10 times higher than in high- z objects with similar Σ_{H_2} . There are some high- z MS galaxies with comparable Σ_{SFR} levels, although they have higher Σ_{H_2} values than IC 4687.
5. Our results suggest that SF is more efficient in IC 4687 than in nearby star-forming galaxies. This agrees with some works that propose the existence of a bimodal SF law. After normalizing the Σ_{H_2} by the global dynamical time, IC 4687 lies in the universal SF law. However, since the local dynamical time does not affect the local SFE, this global dynamical time normalization could be contrived. Alternatively, a normalization using the t_{ff} might recover a universal SF law. The t_{ff} depends on the volume density, therefore, future high spatial resolution observations of dense molecular gas in LIRGs and normal galaxies will reveal whether the local t_{ff} has any influence on the SFE at sub-kpc scales.

Acknowledgements. We thank the referee, Erik Rosolowsky, for his comments, which helped improve this paper. We acknowledge support from the Spanish Plan Nacional de Astronomía y Astrofísica through grants AYA2010-21161-C02-01, AYA2012-32295, AYA2012-39408-C2-1, AYA2012-31447, and FIS2012-32096. This paper makes use of the following ALMA data: ADS/JAO.ALMA#2013.1.00271.S. ALMA is a partnership of ESO (representing its member states), NSF (USA) and NINS (Japan), together with NRC (Canada) and NSC and ASIAA (Taiwan), in cooperation with the Republic of Chile. The Joint ALMA Observatory is operated by ESO, AUI/NRAO and NAOJ. Partially based on observations collected at the European Organisation for Astronomical Research in the Southern Hemisphere, Chile, programmes 077.B-0151A.

References

- Albrecht, M., Krügel, E., & Chini, R. 2007, *A&A*, 462, 575
 Alonso-Herrero, A., Pereira-Santaella, M., Rieke, G. H., & Rigopoulou, D. 2012, *ApJ*, 744, 2
 Alonso-Herrero, A., Rieke, G. H., Rieke, M. J., et al. 2006, *ApJ*, 650, 835
 Alonso-Herrero, A., Rieke, G. H., Rieke, M. J., & Scoville, N. Z. 2002, *AJ*, 124, 166
 Arribas, S., Colina, L., Alonso-Herrero, A., et al. 2012, *A&A*, 541, A20
 Arribas, S., Colina, L., Bellocchi, E., Maiolino, R., & Villar-Martín, M. 2014, *A&A*, 568, A14
 Arribas, S., Mediavilla, E., García-Lorenzo, B., & del Burgo, C. 1997, *ApJ*, 490, 227

- Bellocchi, E., Arribas, S., Colina, L., & Miralles-Caballero, D. 2013, *A&A*, 557, A59
- Bigiel, F., Leroy, A., Walter, F., et al. 2008, *AJ*, 136, 2846
- Bigiel, F., Leroy, A. K., Walter, F., et al. 2011, *ApJ*, 730, L13
- Binney, J. & Tremaine, S. 1987, *Galactic dynamics*
- Bohlin, R. C., Savage, B. D., & Drake, J. F. 1978, *ApJ*, 224, 132
- Bolatto, A. D., Wolfire, M., & Leroy, A. K. 2013, *ARA&A*, 51, 207
- Bothwell, M. S., Chapman, S. C., Tacconi, L., et al. 2010, *MNRAS*, 405, 219
- Briggs, D. S. 1995, PhD thesis, New Mexico Institute of Mining and Technology
- Calzetti, D., Armus, L., Bohlin, R. C., et al. 2000, *ApJ*, 533, 682
- Casasola, V., Hunt, L., Combes, F., & García-Burillo, S. 2015, *A&A*, 577, A135
- Cazzoli, S., Arribas, S., & et al. 2015, submitted
- Cerviño, M., Valls-Gabaud, D., Luridiana, V., & Mas-Hesse, J. M. 2002, *A&A*, 381, 51
- Daddi, E., Elbaz, D., Walter, F., et al. 2010, *ApJ*, 714, L118
- Downes, D. & Solomon, P. M. 1998, *ApJ*, 507, 615
- Fitzpatrick, E. L. 1999, *PASP*, 111, 63
- Gao, Y. & Solomon, P. M. 2004, *ApJ*, 606, 271
- García-Burillo, S., Usero, A., Alonso-Herrero, A., et al. 2012, *A&A*, 539, A8
- Genzel, R., Tacconi, L. J., Gracia-Carpio, J., et al. 2010, *MNRAS*, 407, 2091
- Genzel, R., Tacconi, L. J., Kurk, J., et al. 2013, *ApJ*, 773, 68
- Genzel, R., Tacconi, L. J., Lutz, D., et al. 2015, *ApJ*, 800, 20
- Hodge, J. A., Riechers, D., Decarli, R., et al. 2015, *ApJ*, 798, L18
- Hummer, D. G. & Storey, P. J. 1987, *MNRAS*, 224, 801
- Kennicutt, R. C. & Evans, N. J. 2012, *ARA&A*, 50, 531
- Kennicutt, Jr., R. C. 1998, *ApJ*, 498, 541
- Kennicutt, Jr., R. C., Calzetti, D., Walter, F., et al. 2007, *ApJ*, 671, 333
- Krajinović, D., Cappellari, M., de Zeeuw, P. T., & Copin, Y. 2006, *MNRAS*, 366, 787
- Kroupa, P. 2001, *MNRAS*, 322, 231
- Kruijssen, J. M. D. & Longmore, S. N. 2014, *MNRAS*, 439, 3239
- Krumholz, M. R. & McKee, C. F. 2005, *ApJ*, 630, 250
- Leitherer, C., Schaerer, D., Goldader, J. D., et al. 1999, *ApJS*, 123, 3
- Leroy, A. K., Walter, F., Brinks, E., et al. 2008, *AJ*, 136, 2782
- Leroy, A. K., Walter, F., Sandstrom, K., et al. 2013, *AJ*, 146, 19
- Liu, G., Koda, J., Calzetti, D., Fukuhara, M., & Momose, R. 2011, *ApJ*, 735, 63
- McKee, C. F. & Ostriker, E. C. 2007, *ARA&A*, 45, 565
- McMullin, J. P., Waters, B., Schiebel, D., Young, W., & Golap, K. 2007, in *Astronomical Society of the Pacific Conference Series*, Vol. 376, *Astronomical Data Analysis Software and Systems XVI*, ed. R. A. Shaw, F. Hill, & D. J. Bell, 127
- Onodera, S., Kuno, N., Tosaki, T., et al. 2010, *ApJ*, 722, L127
- Papadopoulos, P. P., van der Werf, P., Xilouris, E., Isaak, K. G., & Gao, Y. 2012, *ApJ*, 751, 10
- Pereira-Santaella, M., Alonso-Herrero, A., Santos-Lleo, M., et al. 2011, *A&A*, 535, A93
- Pineda, J. L., Goldsmith, P. F., Chapman, N., et al. 2010, *ApJ*, 721, 686
- Piqueras López, J., Colina, L., Arribas, S., & Alonso-Herrero, A. 2013, *A&A*, 553, A85
- Piqueras López, J., Colina, L., Arribas, S., Alonso-Herrero, A., & Bedregal, A. G. 2012, *A&A*, 546, A64
- Piqueras López, J., Colina, L., & et al. 2015, submitted
- Rahman, N., Bolatto, A. D., Wong, T., et al. 2011, *ApJ*, 730, 72
- Rahman, N., Bolatto, A. D., Xue, R., et al. 2012, *ApJ*, 745, 183
- Rawle, T. D., Egami, E., Bussmann, R. S., et al. 2014, *ApJ*, 783, 59
- Rodríguez-Zaurín, J., Arribas, S., Monreal-Ibero, A., et al. 2011, *A&A*, 527, A60+
- Schmidt, M. 1959, *ApJ*, 129, 243
- Schruba, A., Leroy, A. K., Walter, F., et al. 2011, *AJ*, 142, 37
- Schruba, A., Leroy, A. K., Walter, F., Sandstrom, K., & Rosolowsky, E. 2010, *ApJ*, 722, 1699
- Silk, J. 1997, *ApJ*, 481, 703
- Storey, P. J. & Hummer, D. G. 1995, *MNRAS*, 272, 41
- Tacconi, L. J., Neri, R., Genzel, R., et al. 2013, *ApJ*, 768, 74
- Tan, J. C. 2000, *ApJ*, 536, 173
- Verley, S., Corbelli, E., Giovanardi, C., & Hunt, L. K. 2010, *A&A*, 510, A64
- Viaene, S., Fritz, J., Baes, M., et al. 2014, *A&A*, 567, A71
- Whitaker, K. E., van Dokkum, P. G., Brammer, G., & Franx, M. 2012, *ApJ*, 754, L29
- Yao, L., Seaquist, E. R., Kuno, N., & Dunne, L. 2003, *ApJ*, 588, 771